


ORIGINAL RESEARCH

Open Access



Comparison of tracer kinetic models for ^{68}Ga -PSMA-11 PET in intermediate-risk primary prostate cancer patients

Nathaniel J. Smith^{1,2*} , Mark A. Green¹, Clinton D. Bahler¹, Mark Tann¹, Wendy Territo¹, Anne M. Smith³ and Gary D. Hutchins¹

Abstract

Background ^{68}Ga -PSMA-11 positron emission tomography enables the detection of primary, recurrent, and metastatic prostate cancer. Regional radiopharmaceutical uptake is generally evaluated in static images and quantified as standard uptake values (SUVs) for clinical decision-making. However, analysis of dynamic images characterizing both tracer uptake and pharmacokinetics may offer added insights into the underlying tissue pathophysiology. This study was undertaken to evaluate the suitability of various kinetic models for ^{68}Ga -PSMA-11 PET analysis. Twenty-three lesions in 18 patients were included in a retrospective kinetic evaluation of 55-min dynamic ^{68}Ga -PSMA-11 pre-prostatectomy PET scans from patients with biopsy-demonstrated intermediate- to high-risk prostate cancer. Three kinetic models—a reversible one-tissue compartment model, an irreversible two-tissue compartment model, and a reversible two-tissue compartment model, were evaluated for their goodness of fit to lesion and normal reference prostate time-activity curves. Kinetic parameters obtained through graphical analysis and tracer kinetic modeling techniques were compared for reference prostate tissue and lesion regions of interest.

Results Supported by goodness of fit and information loss criteria, the irreversible two-tissue compartment model optimally fit the time-activity curves. Lesions exhibited significant differences in kinetic rate constants (K_1 , k_2 , k_3 , K_4) and semiquantitative measures (SUV and %ID/kg) when compared with reference prostatic tissue. The two-tissue irreversible tracer kinetic model was consistently appropriate across prostatic zones.

Conclusions An irreversible tracer kinetic model is appropriate for dynamic analysis of ^{68}Ga -PSMA-11 PET images. Kinetic parameters estimated by Patlak graphical analysis or full compartmental analysis can distinguish tumor from normal prostate tissue.

Keywords ^{68}Ga -PSMA-11 PET, Tracer kinetic model, Compartmental model, Graphical model, Patlak analysis, Primary prostate cancer, Dynamic imaging

Background

Prostate cancer has an estimated lifetime incidence of 1 in every 9 men, but it is estimated that between 20 and 40% of serum PSA-motivated prostate cancer evaluations reflect low-grade, non-malignant changes [1, 2]. Surgery and radiotherapy significantly reduce the prevalence of metastatic disease progression, but may also cause erectile dysfunction and/or urinary incontinence [3]. Appropriately specific diagnostics can reduce the incidence of

*Correspondence:

Nathaniel J. Smith
smithnaj@iu.edu

¹ Indiana University School of Medicine, 950 West Walnut Street, Indianapolis, IN 46202, USA

² Weldon School of Biomedical Engineering, Purdue University, West Lafayette, IN, USA

³ Siemens Medical Solutions USA, Inc., Knoxville, TN, USA

overtreatment and improve patient-specific outcomes. Positron emission tomography (PET) imaging with the urea-based prostate-specific membrane antigen (PSMA) targeted ^{68}Ga -Glu-NH-CO-Lys-(Ahx)-HBED-CC (^{68}Ga -PSMA-11) has greatly improved the diagnosis and treatment planning for prostate cancer, as upregulated PSMA expression has been linked with aggressive or advanced disease [4, 5].

The ^{68}Ga -PSMA-11 tracer standardized uptake value (SUV) correlates with pathological Gleason grade and can support surgical planning as well as detect nodal metastases and biochemical recurrence [6, 7]. SUVs are commonly favored for their ease of clinical implementation, but SUVs depend on accurate dose and scanner cross-calibration, the time between injection and imaging, image acquisition characteristics (scanner, scatter/attenuation correction, reconstruction, frame duration), patient weight and radiopharmaceutical distribution characteristics, and may be affected by patient motion or partial volume effects. Additionally, ^{68}Ga -PSMA-11 does not accumulate in muscle or adipose tissue, and SUV body mass normalization may increase the variability of uptake calculations [8]. Differences in acquisition and reconstruction parameters can also make the comparison of SUVs across different patients and acquisition time-points error-prone, especially when numerical cutoffs are used [9].

Kinetic modeling of tracer binding interactions reduces the impact of errors associated with patient weight, uptake timing, and dose calibration [10]. Unlike SUV analysis and simple static images, dynamic PET imaging with ^{68}Ga -PSMA-11 may be used to distinguish physiologic differences in receptor-ligand affinity, receptor availability, and ligand delivery and extraction, which are considered in aggregate with SUV analysis [11]. These physiologic parameters provide additional information which can improve tissue characterization [12, 13]. However, few studies have compared compartmental models for ^{68}Ga -PSMA-11, and there is not a clear consensus for whether a reversible or irreversible two-tissue compartmental model optimally suits ^{68}Ga -PSMA-11 PET data [14, 15].

^{68}Ga -PSMA-11 is rapidly cleared from the blood, and blood metabolite components may be assumed negligible for the compartmental model [16]. This study aimed to verify the findings by Ringheim et al. and confirm the use of an irreversible two-tissue compartment model for ^{68}Ga -PSMA-11 PET analysis [15].

Methods

Patients

Eighteen men with a total of 23 lesions were included in this retrospective evaluation (NCT04936334), after

two patients were removed from the study cohort due to excessive motion during imaging. This study was approved by the institutional review board, and informed consent was obtained for all individuals prior to imaging. Men with histologically-proven prostate cancer who were scheduled for prostatectomy were eligible for this study if they were over the age of 18 and had at least NCCN intermediate-risk disease or 3 cores of at least Gleason 3+4 disease. Patients needed to be able to lay still for the entire 60-min PET/CT scan and were excluded if they had received treatments with ionizing radiation within the past 30 days. Following prostatectomy, all prostates were analyzed as whole-mount pathological specimens by a board-certified pathologist. Whole-mount pathological findings served as the reference standard for regional tissue classification. The study patients had elevated serum PSA values (median 6.8, range 4.1–20.6 ng/mL) and enlarged prostates (median 40.4 mL, range 27.3–89.4 mL) and were primarily white (17/18). The median patient age was 65 (range 52–75), and the median patient body weight was 90.7 kg (range 63.5–132.0 kg). A more complete charting of patient demographics is contained in Table 1.

PET/CT acquisition protocol

Patients received a 55-min dynamic PET scan acquired in list-mode, centered over the pelvis. Images were acquired with a Siemens Biograph Vision 600 Edge scanner (Siemens Healthineers, Knoxville, USA). The ^{68}Ga -PSMA-11 radiopharmaceutical was prepared as previously reported [17, 18]. At the start of the PET scan, patients received a bolus injection of [^{68}Ga]-PSMA-11 (median 183.5 MBq, range 170.6–186.1 MBq), followed by a 10 mL saline flush. PET images were reconstructed with a 3D ordered-subsets expectation maximization (OSEM) algorithm with point-spread function (PSF) and time of flight (TOF) [3i5s, 3.5 mm FWHM spatial resolution, 210 ps temporal resolution, $1.42 \times 1.42 \times 3.0$ mm voxels, 5 mm Gaussian smoothing]. The images were corrected for decay, attenuation, scatter, dead time, random coincidences and were detector-normalized. The PET images were then processed into 40 temporal frames (12×5 s, 12×10 s, 6×20 s, 10×300 s).

Computed tomography (CT) images were acquired sequentially with the PET scan (120 kV peak, 330 ms exposure time, 658 mA tube current, $0.98 \times 0.98 \times 1.00$ mm voxels, 500 mm field of view) using a soft tissue kernel (Br38).

Image analysis

The reconstructed PET/CT images were analyzed by a board-certified nuclear medicine physician and a board-certified urologist using in-house software (*Q-Image*)

Table 1 Patient characteristics, injected doses, and summary pathology classification

Subject	Age	Prostate volume (cc)	PSA (ng/mL)	Subject Weight (kg)	Injected dose (MBq)	Number of lesions	Lesion location (Gleason grade group)
1	69	35.2	9.6	108.4	183.2	1	RTZ (2), RCZ (1)
2	62	36.1	20.6	132.0	180.6	1	LPZ (3)
3	69	60	9.8	76.2	183.5	1	RCZ (4), RPZ (3)
4	69	39.1	5.6	97.5	183.2	1	LPZ (3)
5	63	30	4.2	79.4	181.3	1	LPZ (2)
6	57	28.5	5.6	90.7	170.6	1	RPZ (2)
7	52	27.3	6.2	111.1	171.7	2	RTZ (2), RPZ (2), LTZ (2)
8	57	51	10.8	108.0	182.4	2	LCZ (2), LTZ (2), RPZ (2)
9	64	43.8	4.8	83.9	185.0	1	RPZ (3)
10	66	59.4	18.5	88.5	185.0	1	LPZ (3)
11	53	37.9	9.2	91.2	183.9	1	LCZ (3)
12	69	66.5	8.7	63.5	184.6	1	LPZ (3)
13	60	41.6	4.5	92.1	186.1	1	RPZ (2)
14	75	37.4	6.6	81.7	184.6	1	LPZ (2)
15	58	62.8	6.7	112.0	185.7	1	RPZ (2)
16	66	41.9	6.8	90.7	183.2	2	LCZ (2), RPZ (1)
17	66	89.4	7.3	69.0	184.3	2	RTZ (2), RPZ (2)
18	67	72.6	4.1	88.0	183.5	2	RPZ (2)

PSA—prostate-specific antigen. The lesion locations are described as the anatomical left (L) or right (R) central zone (CZ), transitional zone (TZ), or peripheral zone (PZ) based on postsurgical whole-mount pathology

built using IDL (L3Harris Geospatial, Boulder, CO, USA). Forty cubic millimeter (~ 50 voxel) spherical reference regions of interest (ROIs) were sampled in the central, peripheral, and transitional prostatic zones in the left and right hemispheres. Separate ROIs were also contoured under physician guidance for the index lesion, contralateral reference region, and secondary lesions when present, as shown in Fig. 1. Accuracy of PET region placements in reference prostate and lesion was retrospectively confirmed with post-surgical whole-mount pathology specimens interpreted by a board-certified pathologist. Time-activity curves (TACs) were extracted in Bq/mL units. SUVs were calculated using the final

15 min of the scan, and mean SUV was calculated for each ROI.

Image-derived input function

The image-derived input function (IDIF) was calculated using in-house software built in IDL. A linear segment of the iliac artery (approximately 20.0 mm) was identified on a bolus phase PET image (approximately the first 60 s of data acquisition). Profiles across the vessel were generated at each location along the length of the vessel that fell within the boundaries of the iliac artery segment. Each profile was fit with a vessel profile model (vessel width step function convolved with scanner resolution

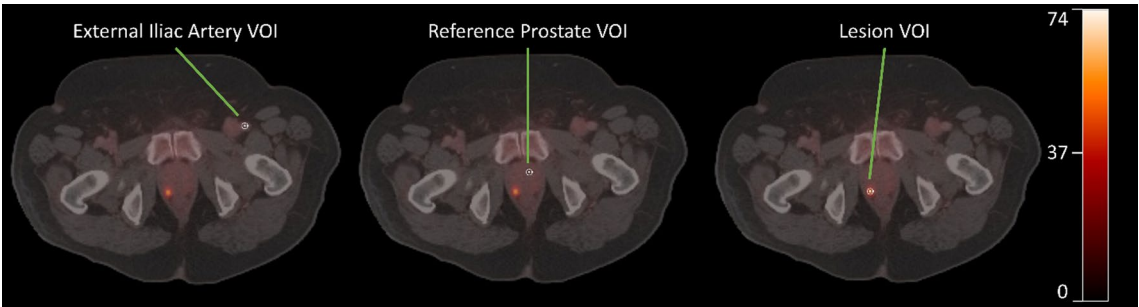


Fig. 1 10 mm spherical VOI placements for artery (left), normal prostate tissue (middle), and lesion (right). An early bolus phase image was used to locate the external iliac artery. All three displayed images are 40–55 min PET frames overlaid with CT. Scale bar is in units of kBq/mL

kernel) to estimate the vessel diameters. The average vessel diameter was then used to generate a 3D vessel model with a background region that was large enough to capture all signal spillover into the vessel region. An arterial input function volume of interest (VOI) was then placed at the center of the vessel region to eliminate resolution distortions that would occur near the edges of the vessel segment. Simulated PET images were generated by convolving the 3D vessel and background regions individually, which were used to estimate the contribution of each region to the arterial input function VOI. The individual contributions represented the fraction of the arterial blood signal that contributed to the arterial input function VOI (F_A) and the fraction of the background region signal that contributed to the arterial input function VOI (F_B). The estimation of resolution distortion corrected arterial blood concentration $C_A(t)$ was calculated using the following equation for each image frame where $C_{VOI}(t)$ is the tracer concentration in the arterial input

function VOI, $C_T(t)$ and V_T are the tracer concentration and volume of the combined artery and background region, V_B is the volume of the background region, and V_A is the volume of the arterial input function VOI.

$$C_A(t) = \frac{\frac{C_{VOI}(t)}{F_B} - C_T(t) \frac{V_T}{V_B}}{\left[\frac{F_A}{F_B} - \frac{V_A}{V_B} \right]}$$

An example of the resolution distortion correction algorithm is demonstrated in Fig. 2.

Kinetic analysis and model validation

Three different kinetic models were evaluated in this analysis: a reversible one-tissue compartment model with two-rate constants (1T2k), an irreversible two-tissue compartment model with three-rate constants (2T3k), and a reversible two-tissue compartment model with four rate constants (2T4k). ^{68}Ga -PSMA-11 was assumed to be

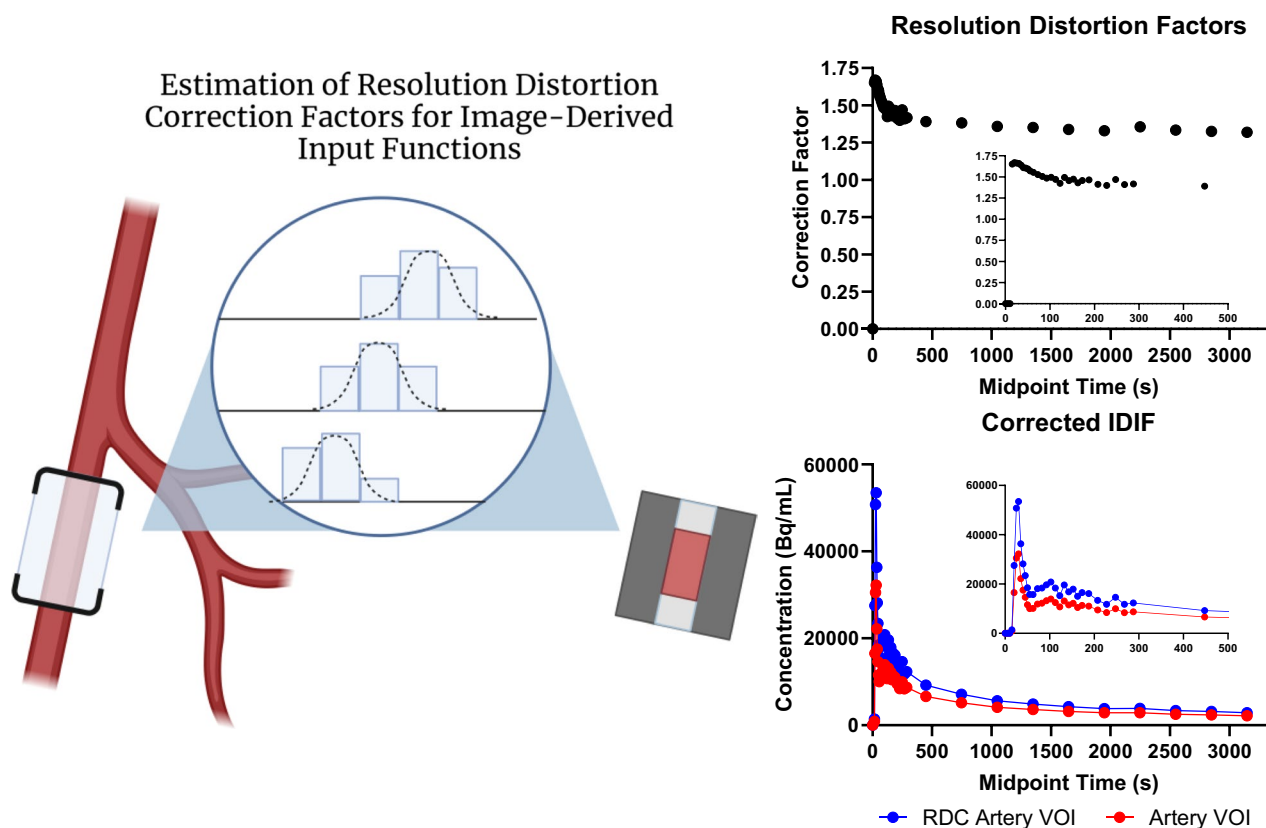


Fig. 2 Representation of the resolution distortion correction method for estimating the IDIF. A 20 mm segment of the iliac artery was manually defined in a region with homogenous background signal. Profiles across the vessel were generated at each location along the length of the vessel segment. Each profile was fit with a vessel profile model to estimate the vessel diameters. The mean vessel diameter estimate was then used to generate a 3D vessel model. Simulated PET images were generated by convolving the 3D vessel and background model to estimate resolution distortion correction factors (shown in upper right for a single patient). Resolution-distortion corrected time-activity curves (lower right) for the vessel region were then generated using the distortion factors and original time-activity curves. IDIF—image-derived input function. RDC—resolution distortion corrected. VOI—volume of interest

Table 2 Parameter definitions

Parameter	Definition	Calculation	Units
K_1	Rate constant, transfer of tracer from plasma to first tissue compartment	Modeled	$\frac{\text{ml}_{\text{blood}}}{\text{ml}_{\text{tissue}} \cdot \text{min}}$
k_2	Rate constant, transfer of tracer from first tissue compartment to plasma	Modeled	min^{-1}
k_3	Rate constant, transfer of tracer from first tissue compartment to second tissue compartment	Modeled	min^{-1}
k_4	Rate constant, transfer of tracer from second tissue compartment to first tissue compartment	Modeled	min^{-1}
K_i	Net tracer influx rate	$K_i = \frac{K_1 k_3}{(k_2 + k_3)}$	$\frac{\text{ml}_{\text{blood}}}{\text{ml}_{\text{tissue}} \cdot \text{min}}$
V_d	Distribution volume of tracer	$V_d = \frac{K_1}{(k_2 + k_3)}$	$\frac{\text{ml}_{\text{blood}}}{\text{ml}_{\text{tissue}}}$
SUV	Standardized uptake value	$\text{SUV} = \frac{C_{\text{PET}}(t)}{\text{Dose}/\text{BodyMass}}$	—
%ID/kg	Percentage of total injected dose per kilogram of tissue	$\% \text{ID}/\text{kg} = \frac{C_{\text{PET}}(t)}{\text{Dose}}$	—

uniformly distributed in plasma with no uptake into red blood cells. Whole blood was weighted by an assumed 38% hematocrit, and no metabolite components were included [15]. Model optimality was evaluated based on chi-square goodness-of-fit criteria and the Akaike information criterion (AIC), consistent with other studies [9]. The 2T3k model net influx rate $K_i = K_1 k_3 / (k_2 + k_3)$ and distribution volume $V_d = K_1 / (k_2 + k_3)$ were evaluated from the full compartmental model as well as the Patlak graphical method [19]. A full tabulation of model parameters can be found in Table 2.

Statistical analysis

Statistical tests were performed with GraphPad Prism 9.5.0 (GraphPad, San Diego, California, USA). Significance was set at 5%, and all variables are reported with median and range or mean and standard deviation. The distributions of all numerical variables were tested for normality. Kinetic and semiquantitative parameters were

compared for lesion, and reference tissue regions using a patient-wise paired Šidák’s test for multiple comparisons. Linear models and Pearson correlations were calculated to assess the association between compartmental parameters, Patlak graphical parameters, and SUVs. The kinetic models were compared for goodness of fit across the central, transitional, and peripheral prostate, and kinetic parameters were compared for consistency across the three prostate zones.

Results

Model selection

Example VOI placements for artery, reference prostate, and lesion are shown in Fig. 1. A sample extracted TAC and modeled curve fits are demonstrated for a lesion and reference prostate in Fig. 3. Chi-square goodness of fit and AIC values for the 1T2K, 2T3K, and 2T4K compartmental models are shown in Fig. 4. All three models performed similarly for prostate and reference tissue

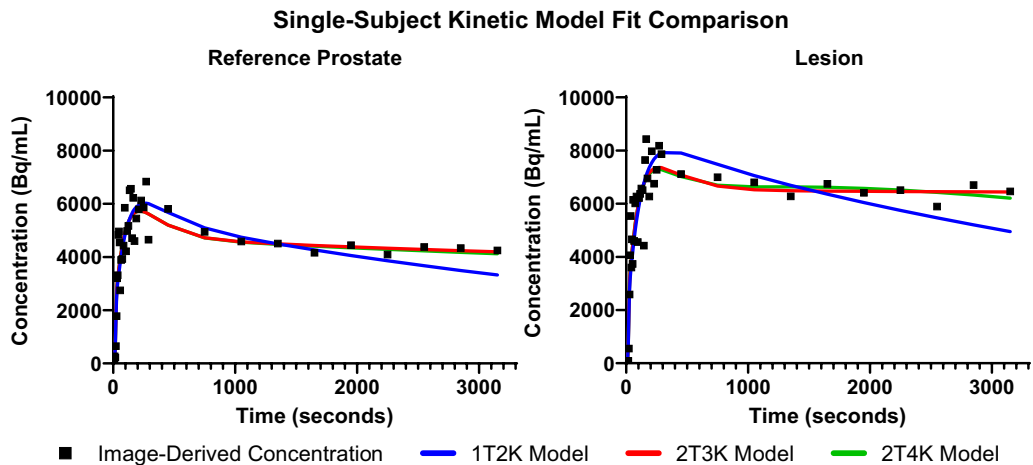


Fig. 3 Comparison of three tracer kinetic model fits for the reference prostate and two lesions originating from subject 17. Model configurations include a one-tissue (1T) and two-tissue (2T) compartment model, with two, three, or four parameters (2K, 3K, 4K, respectively). SUV for the lesion was 3.0

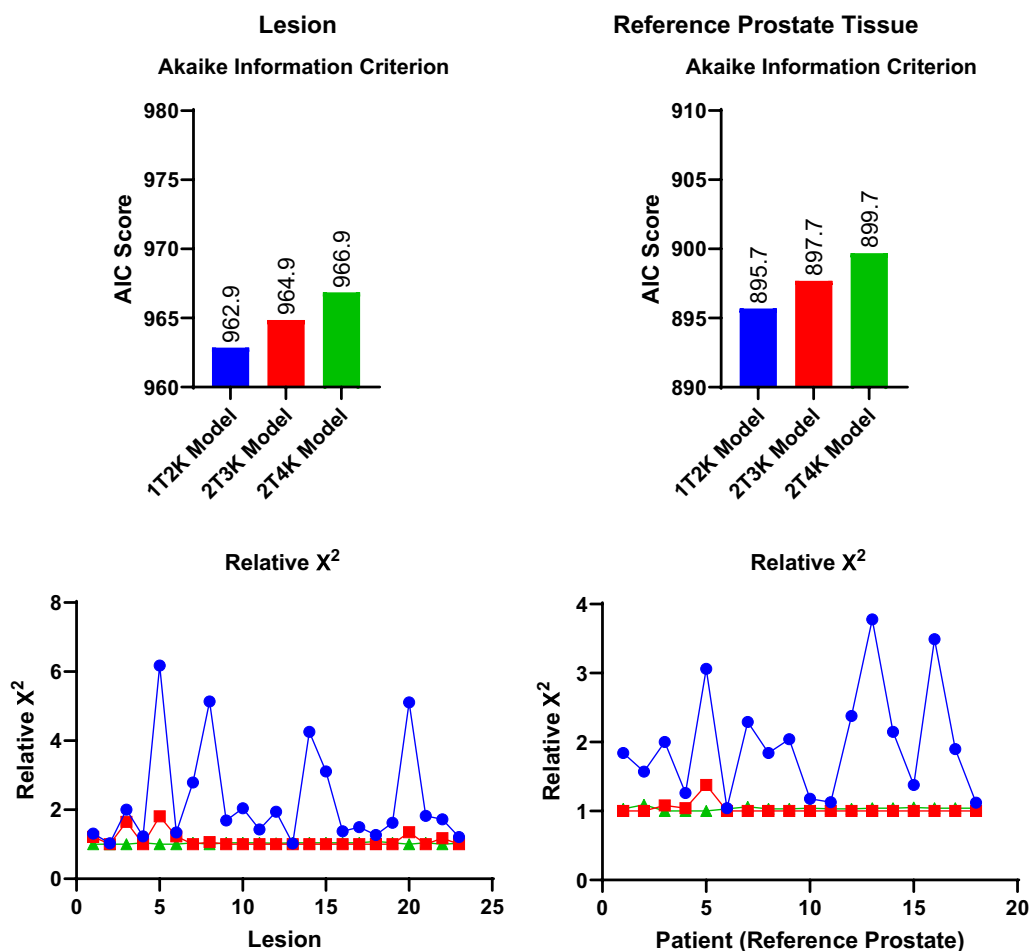


Fig. 4 Model selection criteria for three ^{68}Ga -PSMA-11 tracer kinetic models. Blue refers to the one-tissue compartment, two rate constant (1T2K) model. Red shows the two-tissue compartment, three parameter (2T3K) model, and green shows the two-tissue compartment, four parameter (2T4K) model. Relative X^2 goodness-of-fit values are normalized to the model with the minimal X^2 values for each patient

regions, with a ΔAIC of 2.0 for the 2T3K model and a ΔAIC of 4.0 for the 2T4K model, in reference to the 1T2K exchange model. Therefore, despite similar ΔAIC criteria values between successively parametrized models, the 2T4K model did not adequately improve the TAC fit when corrected for additional parameter bias, relative to the 1T2K model according to rules established by Burnham and Anderson [20]. Relative X^2 goodness-of-fit criteria support the use of the 2T3K and 2T4K models, as X^2 is significantly reduced for the 2T3K ($X^2_{\text{diff}} = 14.76$, $df_{\text{diff}} = 1$, $p < 0.001$) and 2T4K ($X^2_{\text{diff}} = 14.43$, $df_{\text{diff}} = 1$, $p < 0.001$) models relative to the 1T2K model, but not relative to each other ($X^2_{\text{diff}} = 0.33$, $df_{\text{diff}} = 1$, $p = 0.564$). Therefore, the combination of AIC and X^2 goodness-of-fit criteria favors the use of the 2T3K model for ^{68}Ga -PSMA-11.

Parametric evaluation

An assessment of lesion and reference prostate parameter correlations is shown in Fig. 5. Strong correlations were observed between K_1 and V_d for reference prostate tissue (Pearson $r = 0.82$). Additionally, the net influx rate, K_i , demonstrated a strong correlation (Pearson $r > 0.7$) with SUV in reference prostate and lesions, whether it was calculated by full compartmental analysis or Patlak graphical analysis. Accordingly, the Pearson correlation between the compartmental model K_i and Patlak graphical model K_i was 0.91 in reference prostate and lesion. However, there was a moderate positive correlation between the full compartmental model V_d and the Patlak model V_d , especially within the reference prostate (Pearson $r = 0.61$). In lesions, compartmental model rate constants were uncorrelated or weakly correlated with uptake measures (K_p , SUV, Patlak K_p , Pearson $|r| < 0.4$).

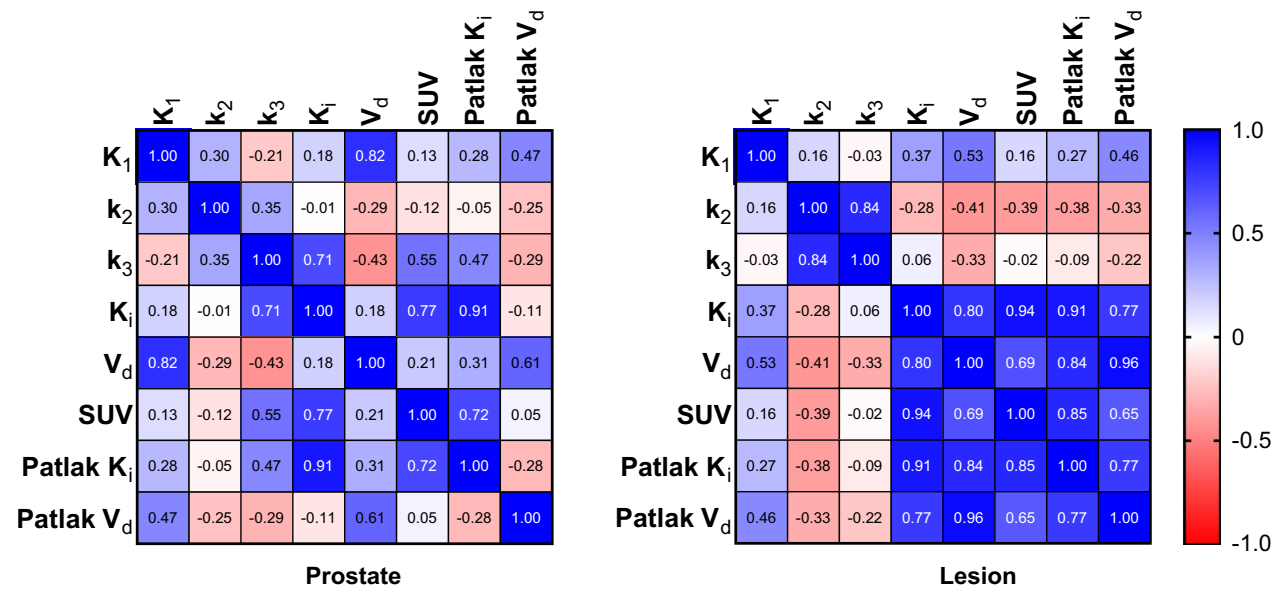


Fig. 5 Pearson parameter correlation matrices for reference prostate ($N=18$) and lesion ($N=23$) volumes of interest

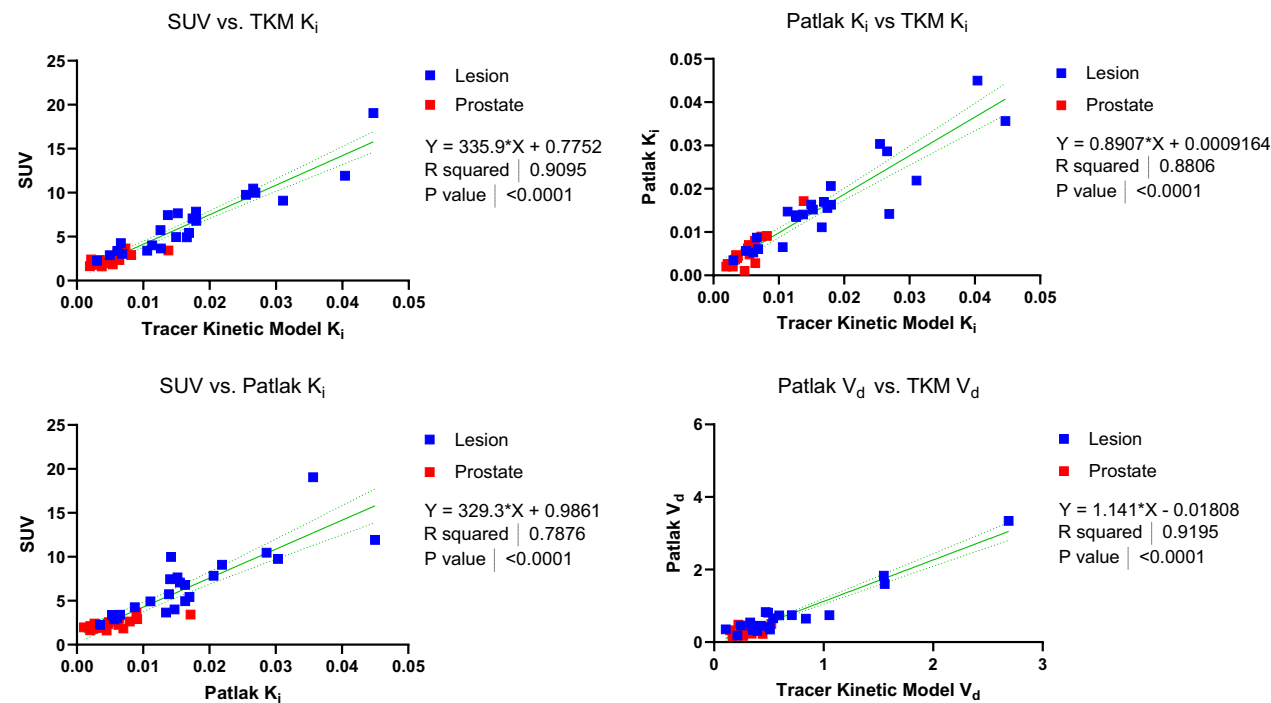


Fig. 6 Linear relationships between kinetic parameters, including both reference prostate and lesion volumes of interest. Linear regression results (equation shown) are displayed as a solid green line, with 95% confidence bands in dashed green. P values indicate a test of significant non-zero regression slope

Linear regressions between SUV, K_i , Patlak K_i , V_d , and Patlak V_d are shown in Fig. 6 and Additional file 1: Fig. S1 for combined lesion and prostate, demonstrating large coefficients of determination between SUV, K_i , and Patlak

K_i . However, differential uptake patterns can be observed between SUV and Patlak K_i images, as shown in Fig. 7.

SUV and %ID/kg serve as measures of ^{68}Ga -PSMA-11 accumulation in static images, but quantification of

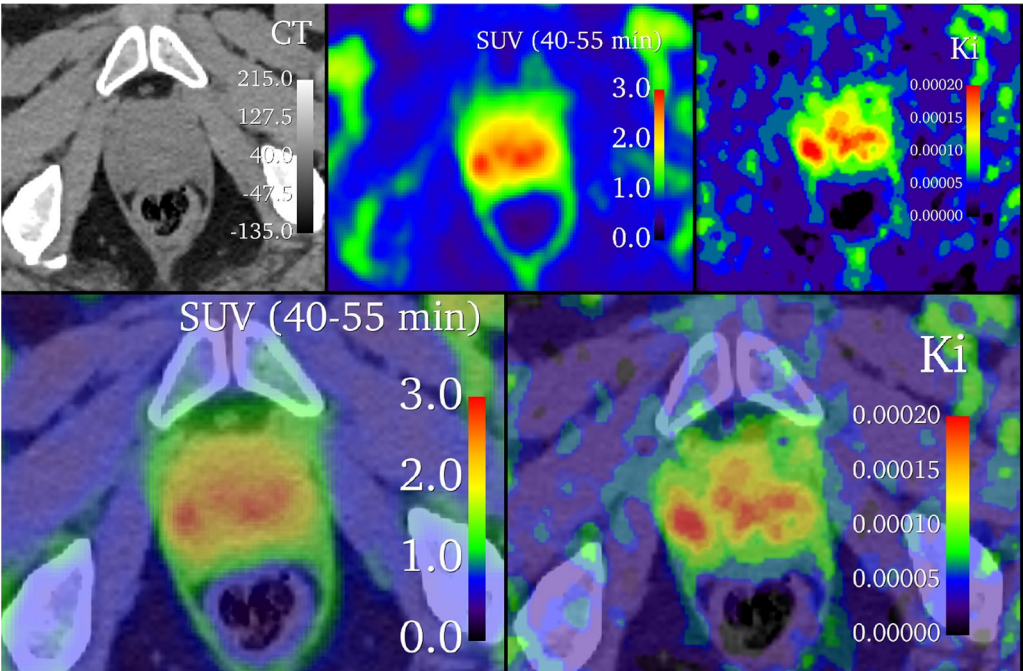


Fig. 7 Comparison of SUV and Patlak K_i ^{68}Ga -PSMA-11 images. The top row shows parametric images alone, and the bottom row is overlaid with CT at 50% opacity

Table 3 Median parameter values from 23 lesions in 18 patients

Parameter	Lesion (n = 23)	Reference prostate (n = 18)
SUV	5.73 [6.74 ± 3.83, 3.84–8.47]	2.34 [2.36 ± 0.59, 1.91–2.65]
%ID/kg	6.64% [7.21 ± 3.47%, 4.77%–8.74%]	2.59% [2.58 ± 0.50%, 2.35%–2.91%]
K_1	0.112 [0.123 ± 0.058, 0.087–0.137]	0.089 [0.090 ± 0.034, 0.075–0.104]
k_2	0.182 [0.247 ± 0.245, 0.110–0.292]	0.317 [0.317 ± 0.094, 0.254–0.369]
k_3	0.032 [0.035 ± 0.029, 0.019–0.038]	0.020 [0.020 ± 0.010, 0.011–0.026]
K_i	0.0152 [0.0174 ± 0.0108, 0.0109–0.0217]	0.0052 [0.0052 ± 0.0028, 0.0033–0.0063]
V_d	0.471 [0.653 ± 0.580, 0.360–0.652]	0.266 [0.278 ± 0.095, 0.205–0.325]
Patlak K_i	0.0147 [0.0165 ± 0.0102, 0.0099–0.0188]	0.0047 [0.0054 ± 0.0038, 0.0028–0.0070]
Patlak V_d	0.458 [0.741 ± 0.688, 0.403–0.742]	0.266 [0.281 ± 0.101, 0.193–0.329]

Shown are comparative median, mean ± standard deviation, first, and third quartile parameter values in lesions and reference prostate tissue. SUV and %ID/kg values are from static images of data from 40 to 55 min post-injection

Shown are median [mean ± standard deviation, first quartile—third quartile] value comparisons for lesion and normal prostate. Semiquantitative values include the standard uptake value (SUV) and percent injected dose per kilogram (%ID/kg). Quantitative parameters include the kinetic two-tissue, three-rate constant model parameters, net influx rate (K_i), distribution volume (V_d), Patlak model net influx rate (Patlak K_i), and Patlak distribution volume (Patlak V_d)

uptake with %ID/kg yielded less variance than with SUV for both tumor and reference prostate (Table 3). For tumors, mean SUV was 6.7 ± 3.8 , while mean %ID/kg was 7.2 ± 3.5 . In normal prostate, mean SUV was 2.4 ± 0.6 vs. a mean %ID/kg value of 2.6 ± 0.5 . In both cases, the mean %ID/kg is higher than SUV, while the variance in %ID/kg is reduced relative to SUV.

Median, mean ± standard deviation, and first and third quartile parameter values are charter for reference prostate tissue and lesions in Table 3. Patient-matched lesion

and reference prostate parameter values are displayed in Additional file 1: Fig. S2. Significant differences between parameter values for lesion and reference prostate are noted for K_1 , k_2 , k_3 , K_i , and SUV in Table 4, while no significant differences in K_i and V_d estimates were observed between compartmental and Patlak models. Additionally, temporal variations in normal prostate and lesion SUV are compared in Fig. 8, demonstrating a plateau in uptake from 30 to 55 min post-injection. Despite parametric differences between lesion and reference prostate,

Table 4 Comparison of semiquantitative and quantitative parameter values between reference prostate and lesion

Šídák's multiple comparisons test	Summary	Adjusted P Value
Reference Prostate K_1 vs. Lesion K_1	**	0.0080
Reference Prostate k_2 vs. Lesion k_2	**	0.0084
Reference Prostate k_3 vs. Lesion k_3	**	0.0080
Reference Prostate K_i vs. Lesion K_i	****	< 0.0001
Reference Prostate V_d vs. Lesion V_d	****	< 0.0001
Reference Prostate SUV vs. Lesion SUV	****	< 0.0001
Reference Prostate Patlak K_i vs. Lesion Patlak K_i	****	< 0.0001
Reference Prostate Patlak V_d vs. Lesion Patlak V_d	****	< 0.0001
Reference Prostate K_i vs. Prostate Patlak K_i	ns	> 0.9999
Reference Prostate V_d vs. Prostate Patlak V_d	ns	> 0.9999

Significance level is set at 0.05 and is corrected for multiple comparisons with the Šídák correction. ns indicates nonsignificant p value greater than the significance threshold. $p < 0.01$ is indicated by **, and $p < 0.0001$ is indicated by ****

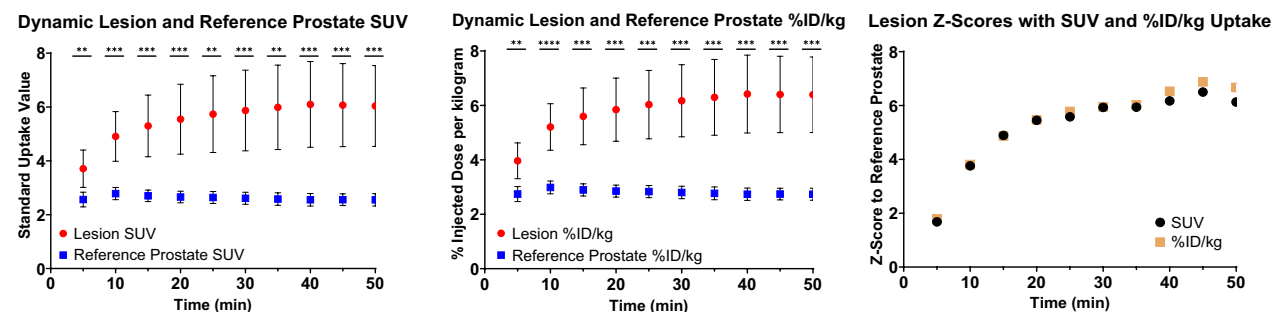


Fig. 8 Comparison of standard uptake value (SUV) temporal trends (left) and %ID/kg temporal trends (right) in normal prostate (blue) and lesion (red). Shown is the mean uptake for prostate and lesion at 5 min intervals, calculated as the uptake over a sliding 10-min window centered over each timepoint. Lesion Z-scores (right) are calculated for SUV and %ID/kg using the difference of lesion signal and reference prostate signal, relative to the standard deviation in reference prostate using patient population averages at each timepoint. Error bars represent 95% confidence intervals of the mean. Statistical tests convey the results of a patient-wise paired t test at each timepoint. $p < 0.01$ is indicated by **, $p < 0.001$ is indicated by ***, and $p < 0.0001$ is indicated by ****

no significant differences in zone-specific kinetic rate constants or model goodness of fit were observed (Additional file 1: Figs. S3 and S4).

Discussion

The results of this study support the use of a two-tissue, three-parameter kinetic model for characterizing the pharmacokinetics of the ⁶⁸Ga-PSMA-11 radiopharmaceutical. ⁶⁸Ga-PSMA-11 exhibits free binding to the extracellular domain of PSMA and slow cellular internalization [21, 22], thus providing a physiological basis for the irreversible two-tissue compartment model and Patlak analysis. Patlak analysis generates estimates of K_i and V_d through a single linear regression to a subset of late-timepoint data, whereas tracer kinetic modeling uses the full temporal image series to estimate individual kinetic model rate constants. Therefore, tracer kinetic modeling may provide a more robust approach to kinetic analysis

when image data are available from the time of tracer injection.

Although the Akaike information criterion suggested that maximal information was preserved by the 1T2k model, chi-square goodness-of-fit criteria suggested that the 1T2k model did not appropriately fit ⁶⁸Ga-PSMA-11 time-activity curves. Therefore, the 2T3k model is optimal based on dual consideration of the Akaike information criterion and chi-square goodness-of-fit criteria. Previous kinetic evaluations of ⁶⁸Ga-PSMA-11 for primary prostate cancer have supported the 2T3k or the 2T4k kinetic models, but the findings of this study are consistent with the analysis in high-risk patients established by Ringheim et al. [14, 15, 23]. In comparison with other primary evaluations of ⁶⁸Ga-PSMA-11 kinetics, the median PSA of patients reported in this study is reduced (6.8 ng/mL) versus Sachpekidis et al. (24.1 ng/mL) and Ringheim et al. (8.64 ng/mL). Additionally, 11/18 patients possessed favorable intermediate grade

disease, in comparison with the greater proportion of high-risk disease in other kinetics studies [15, 23].

Kinetic parameters (K_1, k_2, k_3, K_i) exhibited significant differences between lesion and reference prostate tissue, as demonstrated by patient-wise comparison (Fig. 6, Additional file 1: Fig. S2) and statistical comparisons (Table 4). The compartmental model rate constants were also consistent with the ranges reported by Ringheim et al., but reduced net tracer influx (K_i) and k_3 in this study likely reflect differences in patient disease severity [15]. Parameter differences between lesion and reference prostate remained significant, regardless of whether K_i estimates were obtained by full compartmental models or Patlak graphical analysis. K_i values obtained through compartmental modeling and Patlak analysis were correlated for reference prostate tissue and lesions (Pearson $r=0.91$).

Consistent with other reports, lesion K_i values correlated strongly with SUV for compartmental (Pearson $r=0.94$) and Patlak (Pearson $r=0.85$) models, indicating that 40–55 min post-injection SUV metrics provide similar information as K_i values for lesion detection [15, 23]. Maximal SUVs have also been found to correlate with immunohistochemical PSMA expression and histopathology in patients with prostate cancer [24, 25]. Therefore, it is unlikely that K_i provides additional information beyond that of either the percentage of the injected dose per kilogram or the measured SUV, simpler methods which are readily implemented in many clinical workflows. Instead, further studies are required to assess if K_i -based images have utility in imaging of cancers with lower levels of PSMA expression or in the early detection of disease, where improvements in lesion-to-normal tissue contrast, as demonstrated in Fig. 7, may be more impactful toward differentiating lesions from the image background.

Although K_i (Patlak and full compartmental analysis) correlated strongly with SUV, individual compartment rate constants (K_1, k_2, k_3) demonstrated minimal to slightly negative correlation with SUV. Table 2 and Table 4 demonstrate that K_1 and k_3 are significantly elevated in lesions, while k_2 is significantly decreased. These findings are consistent with increased PSMA expression and PSMA-11 internalization on the prostatic epithelium. The relative reduction in k_2 in lesions conflicts with previous reported trends [15]. However, the high overall estimation variance across all tracer kinetic parameters likely reflects the heterogeneity of prostate cancer across subjects in this study. The analyzed lesions ranged from Gleason Grade Group 1 to 4, representing a greater focus on intermediate-risk disease than in previous studies, possibly contributing to the observed differences.

Table 3 and Fig. 8 demonstrate that relative to SUV, the %ID/kg has reduced parameter variance. Thus, in quantification of ^{68}Ga -PSMA-11 uptake, body mass normalization in the SUV calculation introduces biological noise that reduces diagnostic utility. These observations indicate that ^{68}Ga -PSMA-11 uptake quantification as %ID/kg is preferred when using ^{68}Ga -PSMA-11 PET uptake thresholds for discrimination of disease. Additionally, reference prostate and lesion uptake plateaus beyond 30 min, with peak lesion-to-reference prostate z-scores occurring at 45 min post-injection. Although discordant with EANM/SNMMI ^{68}Ga -PSMA-11 image acquisition guidelines, this finding supports reports indicating that tumor visibility is improved in the 30–45 min window [15, 26–30]. With stable tracer uptake during the 30–55 min window, optimal image acquisition depends largely on count statistics and operational logistics rather than time of acquisition in the first hour post-injection.

As illustrated in Additional file 1: Figs. S3, S4, there were no statistically significant differences between compartmental rate constants, compartmental model K_i , or V_d between normal prostatic tissue in the central, transitional, and peripheral prostatic zone. Additionally, the chi-square goodness-of-fit criterion was consistent across all prostatic zones, indicating that the model is appropriate regardless of prostatic location. This observation is in contrast to previously reported findings by Pizzuto et al. [31] who reported that ^{68}Ga -PSMA-11 accumulation is higher in the central zone than in the transition or peripheral zone. However, the finding was reported during staging for high-risk disease and thus could be attributable as a feature of aggressive disease. In our study, 11% (2/18) patients met or exceeded the average SUV_{mean} reported by Pizzuto et al. in the central zone.

Pelvic ^{68}Ga -PSMA-11 dynamic PET scans are challenging to analyze because the iliac arteries are small in caliber compared to larger ventricular blood pools. In this study, a resolution distortion correction method was employed to estimate the artery blood input function based upon the 3-dimensional imaging characteristics of the PET scanner and the local tissue geometry around a segment of the iliac artery. As a retrospective study, arterial blood samples were not available to use as a reference standard to validate the resolution distortion correction method in these patient studies. The resolution distortion correction algorithm was applied to each frame in the dynamic image sequence to generate an arterial blood input function. This method assumed that the background region surrounding the selected vessel segment was homogeneous. Contamination of the background region from small vessel branches or non-homogenous tissues in the proximity of the vessel would result in

biased correction factors. For this study, iliac artery segments were carefully selected in each patient to minimize background region contamination from adjacent tissues. Since the vessel and background VOI model were defined on an early phase image, patient motion would potentially impact the accuracy of the estimated correction factors.

This study, although consistent with other literature reports in its findings, has several limitations which should inform its interpretation. The patients enrolled in this study all had biopsy-proven disease, and therefore, no healthy control patients were included in the study. Reference prostate was sampled contralaterally to lesions under the guidance of board-certified physicians with knowledge of post-surgical pathology, minimizing the risk of microscopic disease invasion of control tissue. Despite a limited sample size, the study still provided statistical power to suggest optimal model configuration and kinetic parameter differences between lesion and reference prostate. Additionally, the scope of patients included in this study is primarily limited to intermediate-risk disease, and only patients who were candidates for prostatectomy received ^{68}Ga -PSMA-11 PET/CT scans. The study included no low-risk patients, and only a single high-risk patient. Additionally, the demographics of patients meeting the study risk criteria were highly racially homogeneous. The present study was performed on presurgical research scans and did not acquire list-mode data past 55 min. Thus, the kinetics and late time-frame SUV images are temporally constrained and do not fully probe the timeframes recommended by EANM and SNMMI [26].

Conclusion

The two-tissue compartment model with irreversible binding is appropriate for kinetic analysis in ^{68}Ga -PSMA-11 imaging and is applicable to central, transitional, and peripheral prostate, regardless of tumor involvement. Kinetic parameters (K_1 , k_2 , k_3) are useful for distinguishing prostate cancer lesions from normal prostatic tissue, and kinetic parameters provide information about tissue physiology that is independent from SUV-based metrics and Patlak (K_i) net influx rate. Assessment of static images with %ID/kg reflects tumor uptake with less intrinsic variance than SUV.

Abbreviations

PET	Positron emission tomography
PSMA	Prostate-specific membrane antigen
^{68}Ga -PSMA-11	^{68}Ga -Glu-NH-CO-Lys-(Ahx)-HBED-CC
SUV	Standard uptake value
NCCN	National Comprehensive Cancer Network
OSEM	Ordered-subsets expectation maximization

PSF	Point-spread function
TOF	Time of flight
CT	Computed tomography
VOI	Volume of interest
ROI	Region of interest
TAC	Time-activity curve
IDIF	Image-derived input function
1T2K	One-tissue, two-parameter
2T3K	Two-tissue, three-parameter
2T4K	Two-tissue, four parameter
AIC	Akaike information criterion
EANM/SNMMI	European Association of Nuclear Medicine/Society of Nuclear Medicine and Molecular Imaging.
Ref.	Reference

Supplementary Information

The online version contains supplementary material available at <https://doi.org/10.1186/s13550-023-01066-2>.

Additional file 1. Additional supporting figures. Referenced materials include additional parameter regressions (S1), patient-matched parameter values for lesion and reference prostate (S2), comparison of kinetic parameter values by prostatic zone (S3), and reference prostate chi-square goodness-of-fit values by prostatic zone for the 2T3k kinetic model (S4).

Acknowledgements

Not applicable.

Author contributions

All authors contributed to the academic development of the project, approved the final version of the submission, and agreed with the listed order of authorship. NS, MG, CB, MT, AS, and GD contributed to the conception and design of the presented work. NS, CB, MT, WT, and GH contributed to the acquisition and analysis of included datasets. GH designed the analysis software. NS drafted the work, and GH, MT, and AS revised the manuscript prior to submission.

Funding

The authors would like to acknowledge the funding from Siemens Healthineers and NIH R01CA202695 which supported this project. Siemens support provided software licenses for the Vision PET/CT scanner utilized in this report. NIH funds supported salary and research expenses for the reported study design, data collection, analysis, and interpretation.

Availability of data and materials

Data for this publication were acquired in conjunction with NCT04936334. All data and materials presented in this manuscript will be made available upon reasonable request to the corresponding author.

Declarations

Ethics approval and consent to participate

This study was approved by the Indiana University institutional review board (IORG0000134). The study was performed in accordance with the ethical standards as described in the 1964 Declaration of Helsinki and its later amendments.

Consent for publication

Not applicable.

Informed consent

Written informed consent was obtained for all individuals prior to imaging.

Competing interests

The authors declare that they have no competing interests.

Received: 25 October 2023 Accepted: 21 December 2023
Published online: 10 January 2024

References

- Noone A, Howlander N, Krapcho M, Miller D, Brest A, Yu M, et al. SEER Cancer Statistics Review, 1975–2015, National Cancer Institute. SEER. [cited 2022 Dec 17]. Available from: https://seer.cancer.gov/archive/csr/1975_2015/index.html.
- Rawla P. Epidemiology of prostate cancer. *World J Oncol*. 2019;10:63–89.
- Hamdy FC, Donovan JL, Lane JA, Mason M, Metcalfe C, Holding P, et al. 10-Year outcomes after monitoring, surgery, or radiotherapy for localized prostate cancer. *N Engl J Med*. 2016;375:1415–24.
- Bois F, Noirod C, Dietemann S, Mainta IC, Zilli T, Garibotto V, et al. [68Ga] Ga-PSMA-11 in prostate cancer: a comprehensive review. *Am J Nucl Med Mol Imaging*. 2020;10:349–74.
- Sweat SD, Pacelli A, Murphy GP, Bostwick DG. Prostate-specific membrane antigen expression is greatest in prostate adenocarcinoma and lymph node metastases. *Urology*. 1998;52:637–40.
- Chen M, Qiu X, Zhang Q, Zhang C, Zhou Y-H, Zhao X, et al. PSMA uptake on [68Ga]-PSMA-11-PET/CT positively correlates with prostate cancer aggressiveness. *Q J Nucl Med Mol Imaging Off Publ Ital Assoc Nucl Med AIMN Int Assoc Radiopharmacol IAR Sect Soc*. 2022;66:67–73.
- Farolfi A, Calderoni L, Mattana F, Mei R, Telo S, Fanti S, et al. Current and emerging clinical applications of PSMA PET diagnostic imaging for prostate cancer. *J Nucl Med Off Publ Soc Nucl Med*. 2021;62:596–604.
- Demirci E, Sahin OE, Ocak M, Akovali B, Nematyazar J, Kabasakal L. Normal distribution pattern and physiological variants of 68Ga-PSMA-11 PET/CT imaging. *Nucl Med Commun*. 2016;37:1169–79.
- Dimitrakopoulou-Strauss A, Pan L, Sachpekidis C. Kinetic modeling and parametric imaging with dynamic PET for oncological applications: general considerations, current clinical applications, and future perspectives. *Eur J Nucl Med Mol Imaging*. 2021;48:21–39.
- Muzi M, O'Sullivan F, Mankoff DA, Doot RK, Pierce LA, Kurland BF, et al. Quantitative assessment of dynamic PET imaging data in cancer imaging. *Magn Reson Imaging*. 2012;30:1203–15.
- Bailey DL, Townsend DW, Valk PE, Maisey MN. Positron emission tomography: basic sciences. Springer Science & Business Media; 2006.
- Takesh M. The potential benefit by application of kinetic analysis of PET in the clinical oncology. *ISRN Oncol*. 2012 [cited 2020 Dec 4];2012. Available from: <https://www.ncbi.nlm.nih.gov/pmc/articles/PMC3541563/>.
- Kotasidis FA, Tsoumpas C, Rahmim A. Advanced kinetic modelling strategies: towards adoption in clinical PET imaging. *Clin Transl Imaging*. 2014;2:219–37.
- Strauss DS, Sachpekidis C, Kopka K, Pan L, Haberkorn U, Dimitrakopoulou-Strauss A. Pharmacokinetic studies of [68 Ga]Ga-PSMA-11 in patients with biochemical recurrence of prostate cancer: detection, differences in temporal distribution and kinetic modelling by tissue type. *Eur J Nucl Med Mol Imaging*. 2021;48:4472–82.
- Ringheim A, Campos Neto G de C, Anazodo U, Cui L, da Cunha ML, Vitor T, et al. Kinetic modeling of 68Ga-PSMA-11 and validation of simplified methods for quantification in primary prostate cancer patients. *EJNMMI Res*. 2020;10:12.
- Sandgren K, Johansson L, Axelsson J, Jonsson J, Ögren M, Ögren M, et al. Radiation dosimetry of [68Ga]PSMA-11 in low-risk prostate cancer patients. *EJNMMI Phys*. 2019;6:2.
- Green MA, Eitel JA, Fletcher JW, Mathias CJ, Tann MA, Gardner T, et al. Estimation of radiation dosimetry for 68Ga-HBED-CC (PSMA-11) in patients with suspected recurrence of prostate cancer. *Nucl Med Biol*. 2017;46:32–5.
- Bahler CD, Mark G, Hutchins GD, Liang C, Magers MJ, James F, et al. Prostate specific membrane antigen targeted positron emission tomography of primary prostate cancer: assessing accuracy with whole mount pathology. *J Urol*. 2020;203:92–9.
- Patlak CS, Blasberg RG, Fenstermacher JD. Graphical evaluation of blood-to-brain transfer constants from multiple-time uptake data. *J Cereb Blood Flow Metab*. 1983;3:1–7.
- Burnham KP, Anderson DR, editors. Information and likelihood theory: a basis for model selection and inference. *Model Sel Multimodel Inference Pract Inf-Theor Approach*. Springer, New York; 2002. p. 49–97. https://doi.org/10.1007/978-0-387-22456-5_2.
- Eder M, Schäfer M, Bauder-Wüst U, Hull W-E, Wängler C, Mier W, et al. 68Ga-complex lipophilicity and the targeting property of a urea-based PSMA inhibitor for PET imaging. *Bioconj Chem*. 2012;23:688–97.
- Lütje S, Franssen GM, Herrmann K, Boerman OC, Rijpkema M, Gotthardt M, et al. In vitro and in vivo characterization of an 18F-AIF-labeled PSMA ligand for imaging of PSMA-expressing xenografts. *J Nucl Med*. 2019;60:1017–22.
- Sachpekidis C, Kopka K, Eder M, Hadaschik BA, Freitag MT, Pan L, et al. 68Ga-PSMA-11 dynamic PET/CT imaging in primary prostate cancer. *Clin Nucl Med*. 2016;41:e473–9.
- Woythal N, Arsenic R, Kempkensteffen C, Miller K, Janssen J-C, Huang K, et al. Immunohistochemical validation of PSMA expression measured by 68Ga-PSMA PET/CT in primary prostate cancer. *J Nucl Med*. 2018;59:238–43.
- Zamboglou C, Schiller F, Fechter T, Wieser G, Jilg CA, Chirindel A, et al. 68Ga-HBED-CC-PSMA PET/CT versus histopathology in primary localized prostate cancer: a voxel-wise comparison. *Theranostics*. 2016;6:1619–28.
- Fendler WP, Eiber M, Beheshti M, Bomanji J, Ceci F, Cho S, et al. 68Ga-PSMA PET/CT: joint EANM and SNMMI procedure guideline for prostate cancer imaging: version 1.0. *Eur J Nucl Med Mol Imaging*. 2017;44:1014–24.
- Alberts I, Prenosil G, Mingels C, Bohn KP, Viscione M, Sari H, et al. Feasibility of late acquisition [68Ga]Ga-PSMA-11 PET/CT using a long axial field-of-view PET/CT scanner for the diagnosis of recurrent prostate cancer—first clinical experiences. *Eur J Nucl Med Mol Imaging*. 2021;48:4456–62.
- Yu X, Xu L, Li J, Wang Y, Liu J, Chen Y. Optimal 68Ga-PSMA PET/CT imaging in assessment of prostate cancer: feasibility of only delayed acquisition using a total-body PET/CT scanner? *J Nucl Med*. 2022;63:2544–2544.
- Sahlmann C-O, Meller B, Bouter C, Ritter CO, Ströbel P, Lotz J, et al. Biphasic 68Ga-PSMA-HBED-CC-PET/CT in patients with recurrent and high-risk prostate carcinoma. *Eur J Nucl Med Mol Imaging*. 2016;43:898–905.
- Malaspina S, De Giorgi U, Kempainen J, Del Sole A, Paganelli G. 68Ga-PSMA-PET: added value and future applications in comparison to the current use of choline-PET and mpMRI in the workup of prostate cancer. *Radiol Med*. 2018;123:952–65.
- Pizzuto DA, Müller J, Mühlematter U, Rupp NJ, Töpfer A, Mortezaei A, et al. The central zone has increased 68Ga-PSMA-11 uptake: “Mickey Mouse ears” can be hot on 68Ga-PSMA-11 PET. *Eur J Nucl Med Mol Imaging*. 2018;45:1335–43.

Publisher's Note

Springer Nature remains neutral with regard to jurisdictional claims in published maps and institutional affiliations.

Submit your manuscript to a SpringerOpen[®] journal and benefit from:

- Convenient online submission
- Rigorous peer review
- Open access: articles freely available online
- High visibility within the field
- Retaining the copyright to your article

Submit your next manuscript at ► [springeropen.com](https://www.springeropen.com)